Estimation of the remote-sensing reflectance from above-surface measurements

Curtis D. Mobley

The remote-sensing reflectance R_{rs} is not directly measurable, and various methodologies have been employed in its estimation. I review the radiative transfer foundations of several commonly used methods for estimating R_{rs}, and errors associated with estimating R_{rs} by removal of surface-reflected sky radiance are evaluated using the Hydrolight radiative transfer numerical model. The dependence of the sea surface reflectance factor ρ, which is not an inherent optical property of the surface, on sky conditions, wind speed, solar zenith angle, and viewing geometry is examined. If ρ is not estimated accurately, significant errors can occur in the estimated R_{rs} for near-zenith Sun positions and for high wind speeds, both of which can give considerable Sun glitter effects. The numerical simulations suggest that a viewing direction of 40 deg from the nadir and 135 deg from the Sun is a reasonable compromise among conflicting requirements. For this viewing direction, a value of $\rho \approx 0.028$ is acceptable only for wind speeds less than 5 m s^{-1}. For higher wind speeds, curves are presented for the determination of ρ as a function of solar zenith angle and wind speed. If the sky is overcast, a value of $\rho \approx 0.028$ is used at all wind speeds.

OCIS codes: 010.4450, 280.0280, 120.5700, 030.5620.

1. Introduction

The remote-sensing reflectance R_{rs} is widely used in the interpretation of ocean-color data, and well-known formulas [e.g., Eqs. (6), (7), (9), and (10), below] are available to estimate R_{rs} from measurable quantities. The usefulness of these formulas has been established through their successful application in a variety of problems. Nevertheless, some users have only a vague understanding of the formulas' origins in radiative transfer theory and of the assumptions implicit in their use. Consequently, the formulas are sometimes applied with insufficient understanding of their limitations or of the possible errors in R_{rs} resulting from their use. For pedagogical purposes, the theoretical foundations for the estimation of the remote-sensing reflectance are laid out, and some of the errors that can occur in its estimation by use of above-water measurements are quantified.

The author is with Sequoia Scientific, Incorporated, Westpark Technical Center, 15317 NE 90th Street, Redmond, Washington 98052. His e-mail address is mobley@sequoiasci.com.

Received 19 April 1999; revised manuscript received 1 September 1999.

0003-6935/99/367442-14$15.00/0

The remote-sensing reflectance R_{rs} is defined as

$$R_{rs}(\theta, \phi, \lambda) \doteq \frac{L_w(\theta, \phi, \lambda)}{E_d(\lambda)}. \quad (1)$$

Here θ and ϕ specify the polar and azimuthal directions, respectively, in some convenient coordinate system, and λ is the wavelength. $L_w(\theta, \phi, \lambda)$ is the water-leaving spectral radiance in direction (θ, ϕ), that is, the radiance heading upward just above the sea surface that originated from underwater light, which was transmitted upward through the sea surface into direction (θ, ϕ). $E_d(\lambda)$ is the downwelling spectral plane irradiance incident onto the sea surface. The measurements implicit in Eq. (1) are generally made within a few meters of the sea surface and at wavelengths from the near ultraviolet to the near infrared, e.g., for λ from 350 to 800 nm. The λ argument is dropped here for brevity except when necessary for clarity.

Although E_d can be measured directly with commonly available instruments, such a measurement is not possible for L_w. This is because a radiometer pointing toward the sea surface in direction $(\pi - \theta, \pi + \phi)$ measures the sum of the water-leaving radiance $L_w(\theta, \phi)$ plus any incident sky radiance that has been reflected by the sea surface into direction (θ, ϕ). Let L_s denote incident sky radiance (which, when weighted by $\cos\theta$ and integrated over all downward

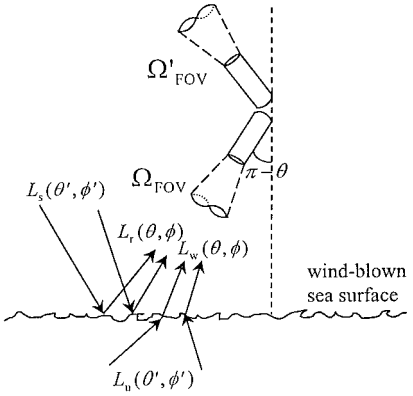

Fig. 1. Illustration of concepts for a wind-blown sea surface. L_r is the surface-reflected part of the incident sky radiance L_s. L_w is the transmitted part of the upwelling underwater radiance L_u. The downward-looking radiometer has a FOV with solid angle Ω_{FOV}.

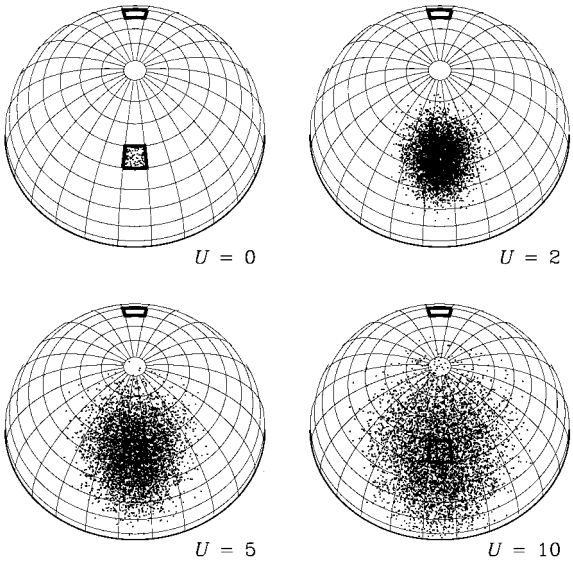

Fig. 2. Illustration of the sky regions seen by a detector looking at the sea surface. U is the wind speed. The detector and specular point are centered at $\theta = 40°$ from the zenith. One hundred points are plotted for $U = 0$, and 5,000 points are plotted for the other cases.

directions, yields E_d), and let L_r denote that part of L_s that is reflected by the sea surface into the direction of the sensor. The total radiance reaching the detector is then

$$L_t(\theta, \phi) = L_r(\theta, \phi) + L_w(\theta, \phi). \quad (2)$$

Because only L_t is directly measurable, it is not possible to compute R_{rs} from direct measurements of the quantities on the right-hand side of Eq. (1). However, the needed L_w can be estimated from $L_w = L_t - L_r$ if an accurate estimate of L_r can be obtained. Any such estimate of L_w then yields an estimate of R_{rs}.

The situation becomes complicated when the sea surface is not level and when the finite field of view (FOV) of the radiometer is taken into consideration. This situation is illustrated in Fig. 1. Sky radiance in any downward direction (θ', ϕ') can in principle be reflected by the wavy surface into the detector. Likewise, upwelling underwater radiance in any upward direction just below the surface, denoted by $L_u(\theta', \phi')$, can be transmitted through the surface and into the detector.

A qualitative feeling for the extent to which sky radiance from various directions can be reflected into a detector can be obtained from Fig. 2. This figure shows the sky hemisphere divided into a (θ, ϕ) grid with a 10-deg spacing in θ and a 15-deg spacing in ϕ. These quadralateral (θ, ϕ) regions are called quads. The two highlighted quads are centered at $\theta = 40$ deg from the zenith direction, which is at the center of the polar cap. The solid angle subtended by these quads is $\Omega = \Delta(\cos\theta)\Delta\phi = (\cos 35° - \cos 45°)(15° \pi/180°) = 0.029$ sr. This corresponds closely to the solid angle seen by a detector with a circular FOV and a 5° half-angle: $\Omega_{FOV} = 2\pi(1 - \cos 5°) = 0.024$ sr.

By use of Monte Carlo techniques described in Mobley[1] (his Section 4.7) and implemented in the Hydrolight 4.0 radiative transfer numerical model,[1–3] rays were generated at random points located in the highlighted quad seen near the top of each panel in Fig. 2. The rays were directed toward a point on the sea surface located directly below the polar cap. The sea surface was modeled as a random surface covered by capillary waves corresponding to a given wind speed U; a different sea surface realization was generated for each initial ray traced. In the case of a level sea surface, $U = 0$, each ray is specularly reflected. Thus all the rays starting in one quad reflect into the conjugate quad, which is speckled by the points showing where 100 reflected rays intersect the grid. For nonzero wind speeds, the capillary wave facets reflect the incident rays into various directions, as illustrated by the $U = 2$, 5, and 10 m s^{-1} cases (which show the results of 5,000 ray tracings and which include multiple scattering by the surface waves). The spread of reflected rays still centers on the specular reflection direction, but a significant number of rays can reflect into directions that are many tens of degrees away from the specular direction, especially at the higher wind speeds.

By reciprocity, any ray starting at one of the plotted points would be reflected into the original quad, i.e., into the sensor. Thus a sensor with a typical FOV, when pointed at a wind-blown sea surface as in Fig. 1, is detecting reflected light from a fairly large part of the sky. If the sky radiance distribution is uniform, then the relative contribution of a given portion of the sky to the detected signal is proportional to the density of plotted points seen in Fig. 2. The actual calculation is complicated by the fact that each reflected ray plotted in Fig. 2 has a different Fresnel reflectance because the ray surface geometry is different for each ray. A nonuniform sky would be represented by a patchy distribution of points: More points in a given portion of Fig. 2 would indicate, for

example, a cumulus cloud that has a greater radiance than the background sky.

2. Theory

The complicated general situation discussed above is described analytically as follows. The total upwelling radiance L_t entering the detector is related to the sky radiance L_s incident onto the sea surface from above and to the upwelling underwater radiance L_u incident onto the sea surface from below by the following exact equation [Mobley[1] Eq. (4.3) averaged over the detector FOV]:

$$\begin{aligned} L_t(\theta, \phi \in \Omega_{\mathrm{FOV}}) = \frac{1}{\Omega_{\mathrm{FOV}}} \int_{\Omega_{\mathrm{FOV}}} \Bigg[\int_{2\pi_d} L_s(\theta', \phi') \\ \times r(\theta', \phi' \rightarrow \theta, \phi) \mathrm{d}\Omega(\theta', \phi') \Bigg] \mathrm{d}\Omega(\theta, \phi) \\ + \frac{1}{\Omega_{\mathrm{FOV}}} \int_{\Omega_{\mathrm{FOV}}} \Bigg[\int_{2\pi_u} L_u(\theta', \phi') \\ \times t(\theta', \phi' \rightarrow \theta, \phi) \mathrm{d}\Omega(\theta', \phi') \Bigg] \mathrm{d}\Omega(\theta, \phi) \\ \equiv L_r(\theta, \phi \in \Omega_{\mathrm{FOV}}) + L_w(\theta, \phi \in \Omega_{\mathrm{FOV}}). \quad (3) \end{aligned}$$

Here Ω_{FOV} is the solid angle of the detector FOV, as illustrated in Fig. 1. The notation $(\theta, \phi \in \Omega_{\mathrm{FOV}})$ denotes the set of (θ, ϕ) directions seen when the detector is pointed toward the sea surface so as to detect radiance in the nominal (θ, ϕ) direction. To be precise, $L_t(\theta, \phi \in \Omega_{\mathrm{FOV}})$ denotes the average radiance over the detector FOV when the detector is pointed in the nominal (θ, ϕ) direction; the total irradiance entering the detector is then $L_t(\theta, \phi \in \Omega_{\mathrm{FOV}})\Omega_{\mathrm{FOV}}$. The hemisphere of all downward directions is denoted by $2\pi_d$, and the hemisphere of all upward directions is denoted by $2\pi_u$. The quantity $r(\theta', \phi' \rightarrow \theta, \phi)$ is the time-averaged radiance reflectance of the sea surface, which tells how much of the incident sky radiance traveling downward in any direction (θ', ϕ') is reflected into any upward direction (θ, ϕ) when observations are made over a time interval long enough to include many periods of the surface waves. The radiance reflectance $r(\theta', \phi' \rightarrow \theta, \phi)$ can be thought of as the time average of the product of the Fresnel reflectance of a wave facet having the orientation that reflects direction (θ', ϕ') into (θ, ϕ) times the probability distribution function for the facet having that orientation. The quantity $t(\theta', \phi' \rightarrow \theta, \phi)$ is the time-averaged radiance transmittance of the sea surface, which tells how much of the upwelling radiance traveling in any upward direction (θ', ϕ') is transmitted through the surface into any upward direction (θ, ϕ). Because the sea surface itself is assumed to be nonabsorbing, Eq. (3) fully accounts for all radiative transfer processes at the sea surface, as regards the total upwelling radiance leaving the surface. Equation (3) generalizes Eq. (2) and is the radiative transfer basis for estimation of the remote-sensing reflectance.

The radiance reflectance $r(\theta', \phi' \rightarrow \theta, \phi)$ and transmittance $t(\theta', \phi' \rightarrow \theta, \phi)$ are inherent optical properties (IOP's) of the sea surface, i.e., their values for a given pair of (θ', ϕ') and (θ, ϕ) directions depend only on the wave state of the sea surface and on the index of refraction of the water, not on the incident radiance distributions. The radiance reflectance and transmittance have units of inverse steradians: They tell what fraction of the incident radiance is reflected or transmitted per unit solid angle. The radiance reflectance and transmittance can be estimated numerically to any desired accuracy for a wind-blown sea surface by use of the Monte Carlo techniques implemented in the Hydrolight 4.0 radiative transfer numerical model.[1–3] The information required for such calculations consists of the wave-slope statistics of the sea surface, which allow mathematical realizations of the sea surface to be generated numerically and used as the basis for Monte Carlo ray tracing, as was done in generating Fig. 2.

Evaluation of the first term on the right-hand side of Eq. (3) requires that the entire sky radiance distribution $L_s(\theta', \phi')$ be measured in conjunction with the sea surface wave state. Evaluation of the second term requires that the upwelling underwater radiance distribution $L_u(\theta', \phi')$ be measured in conjunction with the surface wave state. In principle it is possible to make all these measurements and therefore to evaluate both terms on the right-hand side of Eq. (3). This observation provides two paths to the needed water-leaving radiance L_w. If the sky radiance and wave state are measured, then L_r can be computed and L_w can be obtained from $L_t - L_r$. If the underwater upwelling radiance and wave state are measured, then L_w can be computed directly.

Although it is possible to make the needed measurements of L_s, L_u, and the wave state, doing so on a routine basis would be cumbersome and expensive. In practice, as can be inferred from Fig. 2 (or seen quantitatively in Fig. 4.26 of Mobley[1]), r will be nearly zero for directions far away from the specular reflectance directions of a level sea surface. Thus L_s is needed only for the ranges of (θ', ϕ') for which $L_s r$ is large enough to give a significant contribution to the first integral on the right-hand side of Eq. (3). However, it is difficult to determine *a priori* the relevant region of the sky, especially when the additional effects of gravity waves on the sea surface or of clouds (neither of which were modeled when generating Fig. 2) are considered. Similar statements hold for the directions for which L_u needs to be measured to accurately compute the second integral on the right-hand side of Eq. (3).

3. *Ad Hoc* Formulas

Because of the practical difficulties in evaluating Eq. (3), the two terms on its right-hand side are commonly replaced by simple *ad hoc* formulas. The first

term on the right-hand side of Eq. (3) can be replaced by

$$L_r(\theta, \phi \in \Omega_{\mathrm{FOV}}) \doteq \rho L_s(\theta', \phi' \in \Omega'_{\mathrm{FOV}}). \quad (4)$$

Here ρ is the proportionality factor that relates the radiance measured when the detector views the sky to the reflected sky radiance measured when the detector views the sea surface. The notation $(\theta', \phi' \in \Omega'_{\mathrm{FOV}})$ denotes the directions seen by the radiometer when it is pointed skyward so as to sample the sky radiance that would be specularly reflected by a level sea surface into directions $(\theta, \phi \in \Omega_{\mathrm{FOV}})$, as illustrated in Fig. 1. It is emphasized that, unlike r in Eq. (3), the reflectance factor ρ is not an IOP of the sea surface. In particular, ρ depends not only on direction, wavelength, and wind speed, but also on the detector FOV and on the sky radiance distribution. Although ρ is sometimes[4] called the Fresnel reflectance, this is incorrect terminology: ρ depends on, but in general does not equal, the Fresnel reflectance of the surface at viewing angle (θ, ϕ). Only in the case of a level sea surface and a uniform sky radiance distribution does the integral in Eq. (3) simplify to yield ρ as the average of the Fresnel reflectance over the detector FOV. Equation (4) should be viewed simply as the definition of the nondimensional quantity ρ, whose functional dependence can be expressed as $\rho = \rho(\theta', \phi', \theta, \phi, \lambda, \Omega_{\mathrm{FOV}}$, wind speed, sky radiance distribution). In Sections 4 and 5 I discuss the dependence of ρ on its various parameters.

Although E_d can be measured directly, it is often estimated by one making a radiance reflectance measurement from a gray surface (usually a plaque made of Spectralon), which has a known irradiance reflectance R_g and which is a Lambertian reflector to a good approximation. When an irradiance E_d falls onto a Lambertian surface, the uniform radiance L_g leaving the surface is given by

$$L_g = (R_g/\pi)E_d. \quad (5)$$

L_g can be measured directly when the downward-looking radiometer is kept pointed in the same (θ, ϕ) direction as is used in viewing the sea surface, while the level gray plaque is inserted into the radiometer FOV.

Use of Eqs. (4) and (5) in Eq. (1) yields the equation often used[5] to estimate R_{rs} from the three separate radiance measurements L_t, L_s, and L_g:

$$R_{\mathrm{rs}} = (L_t - \rho L_s) \Big/ \left(\frac{\pi}{R_g} L_g\right). \quad (6)$$

The virtue of using Eq. (6) to estimate R_{rs} is that all measurements are made with the same instrument and, moreover, the instrument does not require an absolute radiometric calibration because any multiplicative error in the three L's will divide out in Eq. (6). Indeed, the radiometer output can be in voltage or digital counts because the factors converting the detector output to radiance divide out. (Any additive error in the radiometer output will presumably be set to zero in the dark-current calibration of the instrument.) R_g is accurately known for substances such as Spectralon, so the successful use of Eq. (6) rests on having an accurate value of ρ.

A variant of Eq. (6) has been adopted as a Sea-viewing Wide Field-of-view Sensor (SeaWiFS) protocol[4] for estimating R_{rs}. This protocol recommends that one first apply Eq. (6), using the Fresnel reflectance at the viewing angle θ for ρ. Under the assumption that the water-leaving radiance is zero at 750 nm, the value of $R_{\mathrm{rs}}(750\ \mathrm{nm})$ can be attributed to residual reflected-sky radiance. Further assuming that the reflected-sky contribution to R_{rs} is independent of wavelength, the protocol then recommends that the $R_{\mathrm{rs}}(\lambda)$ values computed by Eq. (6) be adjusted by subtracting $R_{\mathrm{rs}}(750\ \mathrm{nm})$ from $R_{\mathrm{rs}}(\lambda)$ to obtain the final estimate:

$$R_{\mathrm{rs}}(\lambda; \mathrm{final}) = R_{\mathrm{rs}}[\lambda; \mathrm{by\ (Eq.\ 6)}] - R_{\mathrm{rs}}[750\ \mathrm{nm}; \mathrm{by\ Eq.\ (6)}]. \quad (7)$$

Equations (6) and (7) can be compared as follows. If the correct value for ρ is used at each wavelength, then Eq. (6) gives the correct value for $R_{\mathrm{rs}}(\lambda)$. Equation (7) recognizes that it is difficult to guess the correct ρ and attempts to improve the initial estimate by applying a wavelength-independent correction to R_{rs}. The success of this correction depends on the wavelength dependence of ρ and on whether the water-leaving radiance is actually zero at 750 nm.

Zaneveld[6] recommends on theoretical grounds that the scalar irradiance E_{od} be used in Eq. (1) in place of the plane irradiance E_d. This substitution should remove some of the angular variability in R_{rs} that results from the viewing geometry. However, his recommendation seldom has been employed, possibly because his definition requires a direct measurement of E_{od}. (Note that it is not possible to estimate E_{od} from gray plaque measurements in a manner similar to that described for E_d in Eq. (6). This is because the scalar irradiance reflectance $R_o \doteq E_{\mathrm{ou}}/E_{\mathrm{od}}$ of a Lambertian surface depends on the incident radiance distribution, unlike the plane irradiance reflectance $R = E_u/E_d$, which is independent of the incident lighting for a Lambertian surface. R_o equals R only if the Lambertian gray plaque is isotropically illuminated.) The results to follow apply to either definition of R_{rs}.

The second term on the right-hand side of Eq. (3) can be replaced by

$$L_w(a; \theta, \phi \in \Omega_{\mathrm{FOV}}) \doteq \tau L_u(w; \theta', \phi' \in \Omega_u). \quad (8)$$

Here τ is the nondimensional proportionality factor that relates the upwelling radiance measured by an underwater detector viewing some subset Ω_u of $2\pi_u$ to the water-leaving radiance entering the above-surface detector viewing the sea surface. Depth arguments a (for air) and w (for water) were added to the radiances to remind us that these quantities are being measured on different sides of the sea surface. Like ρ in Eq. (4), τ is not an IOP of the sea surface.

In particular, τ depends not only on direction and sea state, but also on the detector FOV and on the sky and upwelling radiance distributions.

Consider for the moment a level sea surface and infinitesimal detector FOV's. The directions (θ', ϕ') and (θ, ϕ) in Eq. (8) are then related by Snell's law $\sin\theta = n \sin\theta'$, where n is the index of refraction of the water (relative to air) and by $\phi = \phi'$. In this case, Eq. (8) just expresses the n^2 law for radiance propagation across the surface. The τ factor then becomes an IOP that can be identified as

$$\tau = \frac{1 - r_F(\theta', \theta)}{n^2},$$

where $r_F(\theta', \theta)$ is the Fresnel reflectance of the surface as seen from the water side. For $n \approx 1.34$ and for the range of (θ', θ) values relevant to most remote-sensing situations ($\theta < 50$ deg), r_F lies between 0.02 and 0.04, so that τ falls between 0.53 and 0.55. The situation is more complicated for wind-blown sea surfaces and finite FOV's, in which case τ is no longer an IOP and may be more variable, but even then a value of $\tau \approx 0.54$ often may be reasonable.

Equation (8) can be divided by the sky irradiance incident onto the sea surface to obtain

$$R_{\mathrm{rs}}(\theta, \phi) = \tau \frac{L_u(w; \theta', \phi')}{E_d(a)}, \tag{9}$$

where the FOV arguments are dropped for brevity, but an a argument is added to E_d to remind us that this irradiance is being measured in air. A virtue of using Eq. (9) to estimate the remote-sensing reflectance is that no correction for surface-reflected skylight is required, as is the case when Eq. (6) is used. Moreover, commercial instrument packages are available to make the needed measurements.

Equation (9) is often rewritten in terms of in-water quantities by use of the exact radiative transfer relationship [Mobley[1] Eq. (4.6)]:

$$E_d(w) = E_u(w)R_u + E_d(a)(1 - R_s).$$

Here R_u is the irradiance reflectance of the surface (from the water side) for upwelling irradiance, R_s is the irradiance reflectance of the surface (from the air side) for the incident sky irradiance, and E_d and E_u are plane irradiances in the air or water, as shown. The result is

$$R_{\mathrm{rs}}(\theta, \phi) = \left\{\frac{[1 - r_F(\theta', \theta)](1 - R_s)}{n^2(1 - RR_u)}\right\} \times \frac{L_u(w; \theta', \phi')}{E_d(w)} \doteq T \frac{R}{Q(\theta', \phi')}, \tag{10}$$

where T is the quantity in braces, $R = E_u(w)/E_d(w)$, and $Q(\theta', \phi') \doteq E_u(w)/L_u(w; \theta', \phi')$. It should be noted that R_s and R_u depend on their respective radiance distributions and are apparent optical properties, even though they describe the reflectance properties of the air–water surface itself. The subsurface irradiance reflectance R is an apparent optical property of the water body. Note the conceptual difference in R_s, which describes how the surface itself reflects incident sky irradiance, and in the albedo of the sea surface $E_u(a)/E_d(a)$, which is the ratio of total upwelling irradiance (including irradiance transmitted through the surface from the water below) to total downwelling irradiance. A corresponding distinction is made between R_u and R. See Mobley[1] for additional discussion of these surface reflectance quantities.

As already noted, r_F lies between 0.02 and 0.04 for θ' and θ in the angular ranges relevant to most ocean-color sensors. For solar zenith angles less than 60 deg in a clear sky, or for overcast skys, $R_s < 0.07$; $R_s < 0.03$ for solar angles less than 45 deg.[7] For typical underwater light fields, $R_u < 0.7$. R values are typically less than 0.05 and are almost always less than 0.1 (at least in case 1 waters). The bracketed term in Eq. (10), denoted here by T, then falls in the range of 0.50 to 0.57, with a value of 0.54 being typical. The rough numerical equality between τ in Eq. (9) and T in Eq. (10) is to an extent coincidental; τ and T are conceptually different quantities.

Because the value of T varies by only a few percent about the value 0.54, most of the variability in R_{rs} arises from variability in R/Q. The dependence of R/Q on the IOP's of the water body—in particular on the absorption and backscatter coefficients—has been studied by Gordon *et al.*[8] The directional dependence of the Q factor has been numerically studied by Morel and Gentili[9] for various environmental conditions (note that R/Q depends implicitly on the solar zenith angle, sea state, and water IOP's, all of which affect the underwater radiance distribution). Their results are compared with measurements in Morel *et al.*[10] The results of these thorough studies need not be repeated here.

The virtue of one using Eq. (10) to estimate the remote-sensing reflectance is that R_{rs} is obtained entirely from measurements made within the water. As with Eq. (9), there is no need to correct for surface-reflected skylight. On the other hand, the measurements needed to evaluate Eqs. (9) or (10) come with their own difficulties, such as the effects of wave focusing and self-shading on instruments just beneath the sea surface and the need to extrapolate measured values from the depth of measurement to just below the surface. Both Eqs. (9) and (10) require accurately calibrated instruments. The accuracy of Eq. (10) of course rests on one using the correct values for T, R, and Q. Even though the functional dependence of R_{rs} is on the ratio R/Q, R and Q are obtained from separate measurements made by different instruments. Q especially can be estimated inaccurately if L_u is measured with a nadir-directed radiometer and then used to compute R_{rs} at off-nadir directions.

The papers just cited[8–10] have adequately studied the quantities seen in Eq. (10). The remainder of the present paper is therefore devoted to studying

variability in the ρ parameter of Eq. (6), which has received less attention.

4. Dependence of ρ on Viewing Geometry and Wind Speed

The Hydrolight radiative transfer numerical model[1–3] is an ideal tool for investigating the variability of ρ as the sea state and viewing geometry vary. Input to Hydrolight consists of the incident sky radiance distribution, a statistical description of the wind-blown sea surface (usually given as capillary wave-slope statistics parameterized in terms of the wind speed), the absorption and scattering properties of the water itself, and the nature of the water bottom boundary (which may be of finite or infinite depth). The model solves the radiative transfer equation to obtain the full radiance distribution within and leaving the water. The model computes separately the water-leaving radiance L_w and the reflected sky radiance L_r. This makes it possible to evaluate the individual contributions of L_r and L_w to the measurable total upwelling radiance L_t. In particular, Hydrolight can easily compute $\rho = L_r/L_s$ for any given set of environmental conditions or viewing geometry.

The figures in this section show the dependence of ρ on Sun zenith angle, viewing direction relative to the solar position, wind speed, and sky conditions. The Hydrolight model does not include polarization, and therefore these results presume that the detector does not pass the light through a polarizing filter before recording the signal. It should be noted that ρ as discussed here does include the effects of Sun glitter, which may be present in actual measurements.

Most sensors used for field estimation of R_{rs} have an FOV of approximately 10 deg. Therefore Hydrolight was run with a partition of the set of all directions into 10-deg θ and 15-deg φ bands, plus two polar caps with a 10-deg full angle. This partitioning of θ and φ was shown in Fig. 2. As already noted, the solid angles of the θ, φ quads correspond roughly to that of the FOV of a typical instrument. The quads are centered at θ values of 0 (the polar cap), 10, 20, 30 deg and so on. Hydrolight computes the radiance directionally averaged over each of the quads, just as an instrument measures the average radiance within the instrument FOV. When the Sun is placed in a particular quad, say one centered at θ = 30 deg, the Sun is spread out over the θ range from 25 to 35 deg, and over a 15-deg φ range, but the average radiance over the quad is the same as would be measured by an instrument with a 10-deg by 15-deg rectangular FOV when pointed at the Sun.

When one is making field measurements, it is common to orient the radiometer at right angles to the Sun's direction, i.e., in the vertical plane perpendicular to the Sun's azimuthal plane. This is done to minimize the effects of Sun glitter and of ship shadow. In the simulations below, the Sun is at φ = 0. The standard sensor orientation then corresponds to φ = 90 or 270 deg. The viewing geometry is then completely specified by one giving the solar zenith angle θ_s and the viewing angle θ_v, as shown in Fig. 3.

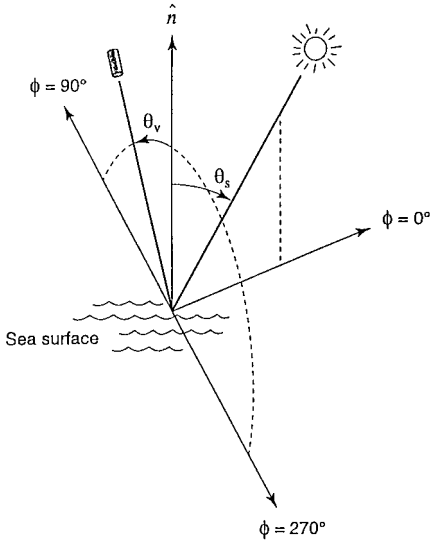

Fig. 3. Sun and sensor geometry as often used in field measurements.

To study the variability of ρ, a series of Hydrolight simulations were made for the following conditions:

Wind speeds of $U = 0$, 2, 5, 10, and 15 m s^{-1} were used to define the random sea surface. The surface was modeled by use of azimuthally averaged Cox–Munk wave-slope statistics appropriate for a sea surface covered by capillary waves. Although an actual capillary wave surface does display some azimuthal asymmetry in the along-wind and cross-wind slopes, the effect of this asymmetry on the surface reflectance is small for solar angles and viewing directions that are not near the horizon.[7] By one using azimuthally averaged slope statistics, only the azimuthal angle between the Sun and the viewing directions needs to be specified; the azimuthal direction of the wind is irrelevant.

The semiempirical sky radiance model of Harrison and Coombes[11] was used to define the angular pattern of the sky radiance distributions incident onto the sea surface. The Sun is placed at the desired zenith angle θ_s, and the remainder of the sky has a nonuniform radiance distribution that is close to that of a real sky on a clear day. The Harrison and Coombes model is based on many observations of sky radiances and includes both Rayleigh- and aerosol-scattering effects. Solar zenith angles of $\theta_s = 0$, 10, 20, . . . , 80 deg were used.

The results of Sections 4 and 5 depend only on the sea surface and sky conditions; they are independent of the water IOP's. Specific water IOP models as needed for the simulations of Section 6 are described in that section. In all cases, the water was taken to be homogeneous and infinitely deep because remote-sensing signals are determined by the near-surface water properties.

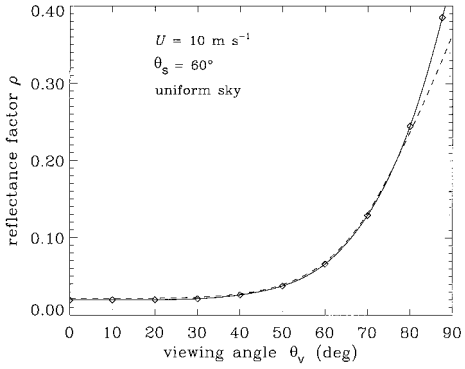

Fig. 4. Comparison of ρ as computed by Hydrolight (solid curve) and by Austin[12] (dashed curve). The wind speed is 10 m s^{-1} and the Sun is at $\theta_s = 60°$ in a uniform background sky.

Austin[12] presents tables of ρ computed for various wind speeds, solar angles, and viewing angles using the Cox–Munk capillary wave-slope statistics. Austin does not describe the manner in which he made his calculations, but presumably he averaged the Fresnel reflectance for a distribution of angles as determined by the Cox–Munk wave-slope statistics. Austin's calculations were made for a uniform sky radiance distribution, and they do not include any specular reflection effects from the Sun's direct beam. Figure 4 shows one set of Austin's tabulated values compared with the corresponding ρ values computed by Hydrolight (using a uniform sky radiance distribution). The wind speed is $U = 10$ m s^{-1} and the Sun zenith angle is $\theta_s = 60$ deg. The plotted curves are spline fits to values computed at θ_v intervals of 10 deg. The agreement is clearly excellent for viewing angles θ_v less than 80 deg. For viewing angles near the horizon, the difference between the Hydrolight and the Austin curves is probably due to multiple scattering by the wave facets, which is included in Hydrolight but presumably not in Austin's calculations.

Austin's report[12] is sometimes cited as the justification for one using a ρ value of roughly 0.02 or 0.03 in Eq. (6). Note that $\rho \approx 0.020$ for viewing angles less than 30 deg, and $\rho \approx 0.028$ for $\theta_v = 40$ deg. However, Austin cautions the reader that his results apply only to a uniform sky radiance distribution and only if the viewing geometry is such that there is no specular reflection of the Sun's direct beam into the sensor FOV.

Actual clear-sky radiance distributions are of course not uniform, and Sun glitter unavoidably may be present when viewing the sea surface. Figure 5 shows a plot like the plots of Fig. 2, but with the clear-sky relative radiance pattern as computed by the Harrison and Coombes[11] formulas superimposed on the reflected-ray pattern (radiances are normalized to one near the Sun's direction). The wind speed was 15 m s^{-1} and the Sun was placed at $\theta_s = 30$ deg at a right angle to the viewing direction; 10,000 rays are plotted. It is clear from the ray pattern and radiance distribution over the sky hemisphere that the sensor is sampling a large part of the sky, for which the background sky radiance varies by over a factor of 10 in magnitude, and that some of the rays come from near the Sun and thus will have large radiances.

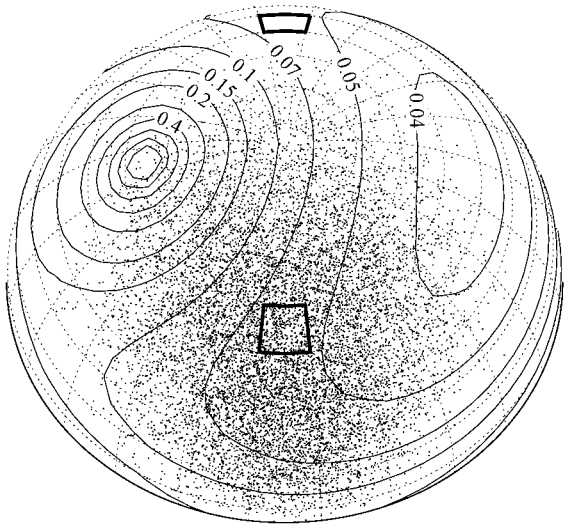

Fig. 5. Illustration of the sky region seen by a detector for $U = 15$ m s^{-1}, as in Fig. 2; 10,000 points are plotted. The solid lines are contours of the relative sky radiance computed by the formulas of Harrison and Coombes[11] for $\theta_s = 30°$ in a clear sky.

Figure 6 shows how Sun glitter and a realistic sky radiance distribution can greatly alter the nominal ρ values seen in Fig. 4. Figure 6 shows ρ as obtained from Hydrolight's input L_s and computed L_r values in Eq. (4) for various Sun zenith angles from 20 to 60 deg. Because the sea surface generation and ray tracing are performed with Monte Carlo techniques, there is statistical noise in the curves of Fig. 6. The dotted curves for $\theta_s = 30$ deg show the results of six independent Monte Carlo simulations, each using 20,000 randomly generated sea surfaces. The

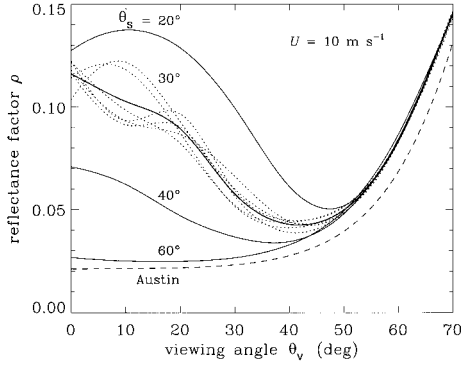

Fig. 6. Effects of Sun glitter and nonuniform sky radiance on ρ. The wind speed is $U = 10$ m s^{-1} and the sky has a radiance distribution characteristic of a clear sky (as in Fig. 5); θ_s is the solar zenith angle. The dotted curves are different Monte Carlo simulations for the $\theta_s = 30°$ case. The dashed curve is Austin's curve from Fig. 4.

Monte Carlo noise is greatest at $\theta_v = 10$ deg because the quads centered at 10 deg have the smallest solid angles and therefore receive fewer reflected rays than do the other quads (recall Fig. 2). The solid curve for $\theta_s = 30$ deg is the average of the six simulations. The curves for the other θ_s values are from only one Monte Carlo simulation. (All curves are plotted from spline fits to the values computed at intervals of $\theta_v = 10$ deg.)

The ρ curve for $\theta_s = 60$ deg in Fig. 6 is noticeably greater than the Austin curve. This is a consequence of the nonuniform sky radiance distribution; recall that Fig. 4 was for a uniform sky radiance. Note that for viewing angles of $\theta_v < 40$ deg, ρ increases as the Sun climbs higher in the sky. This is because Sun glitter cannot be avoided when both θ_s and θ_v are small. If, for example, θ_v is 30 deg—a typical value used in the field—and the Sun is at $\theta_s = 20$ deg, then the correct value of ρ is approximately 0.1, which is over three times the often-used value of 0.028. In practice, an observer would likely notice the glitter in the sensor FOV and would then use a greater viewing angle to avoid the obvious glitter. But even if the observer uses a viewing angle of 40–50 deg, which would minimize the glitter effect, the correct value of ρ is still almost twice the nominal value of 0.028. At viewing angles beyond 50 deg, ρ again rises because of the increase in the Fresnel reflectance of the surface at angles greater than 50 deg. Thus for a 10-m s^{-1} wind and a 20-deg Sun angle, there is no viewing angle for which $\rho \approx 0.028$ would be a good value.

Figure 7 shows contour plots of ρ for $\theta_s = 30$ deg and for $U = 5$ and 10 m s^{-1}. The dotted circles represent lines of constant polar viewing direction: θ_v is 0 at the center and 60 deg at the outer rim of the plots. The azimuthal angle in the plots represents ϕ_v as labeled. The ρ values are contoured at intervals of 0.03, 0.04, . . . , 0.12. The irregular pattern of some of the contour lines near the centers of the plots and at the outer edges is a consequence of the irregular (θ_v, ϕ_v) grid used for contouring and of Monte Carlo noise in ρ for small θ_v values, as mentioned above. Qualitative inspection of these plots suggests that an azimuthal viewing direction of $\phi_v = 90$ deg is not optimum for the purpose of estimating ρ. When one moves from the center of the plots to their top, i.e., when increasing θ_v from 0 to 60 deg while holding ϕ_v constant at 90 deg, ρ tends to remain large until a fairly narrow minimum is reached near $\theta_v = 40$ deg, as was seen in Fig. 6. Note also that a small change in ϕ_v when near $\phi_v = 90$ deg (e.g., making observations at $\phi_v = 80$) can cause a large change in ρ. However, at larger ϕ_v values, ρ decreases more quickly with θ_v and has a broader minimum with lower values than at $\phi_v = 90$ deg. Use of a ϕ_v value of 180 deg might be optimum for estimating ρ but could lead to other problems such as shadowing of the reflectance plaque or glory effects from water backscatter.[4] Therefore a ϕ_v value of ~135 deg from the Sun appears to be a good compromise that would minimize shadowing problems while also giving a better estimate for ρ than can be obtained for $\phi_v = 90$ deg. (Figure 7 also makes it clear that ρ is not equal to the Fresnel reflectance, whose contours would be concentric circles.)

Figure 8 shows ρ as a function of wind speed and θ_v for $\phi_v = 90$ deg (dotted curves) and 135 deg (solid curves) for $\theta_s = 30$ deg as in Fig. 7. The ρ values have a broader minimum and, more importantly, show less dependence on wind speed for $\phi_v = 135$ deg than for $\phi_v = 90$ deg. If observations are made at $\theta_v = 30$ to 40 deg, then for $\phi_v = 135$ deg ρ increases from ~0.025 at low wind speeds to ~0.04 at $U = 15$ m s^{-1}, whereas ρ increases to ~0.08 at 15 m s^{-1} for $\phi_v = 90$. Thus there is a factor of 2 less variability in ρ at $\phi_v = 135$ deg. In a study of the use of polarizers for reduction of surface-reflected skylight, Fougnie *et al.*[13] independently reached this same conclusion, namely, that (θ_v, ϕ_v) near (40°, 135°) is optimum.

Figure 9 shows ρ as a function of wind speed and solar zenith angle θ_s for a viewing angle of $\theta_v = 40$ deg. As in Fig. 8, the solid curves are for $\phi_v = 135$ deg and the dotted curves are for $\phi_v = 90$. Figure 9 can be used to estimate the value of ρ that should be

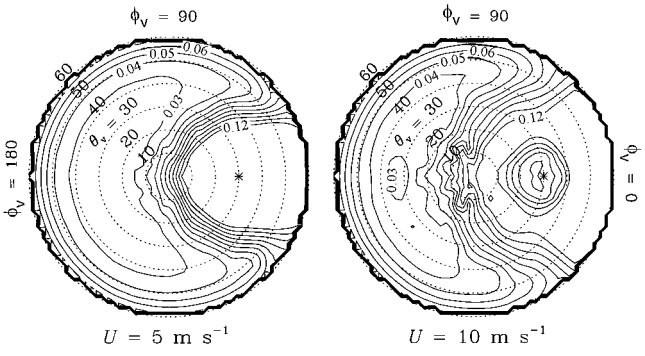

Fig. 7. Contour plots of ρ (solid lines) as a function of viewing direction (θ_v, ϕ_v) for $\theta_s = 30$ deg and two wind speeds. Contour values are 0.03 to 0.12 by 0.01. The ✳ symbols show the specular direction of the Sun, and the θ_v contours (dotted lines) are labeled along the $\phi_v = 135$-deg direction.

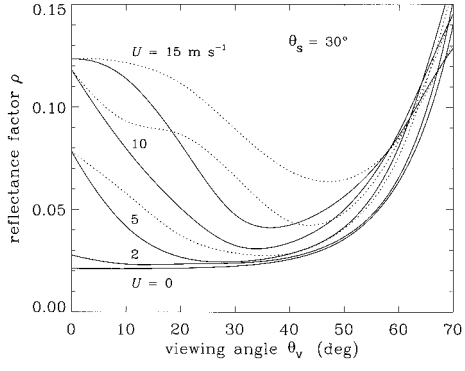

Fig. 8. Effect of wind speed and viewing direction on ρ for a Sun zenith angle of $\theta_s = 30$ deg and a clear-sky radiance distribution. The solid curves are for an azimuthal viewing direction of $\phi_v = 135$ deg, and the dotted curves are for $\phi_v = 90$ deg.

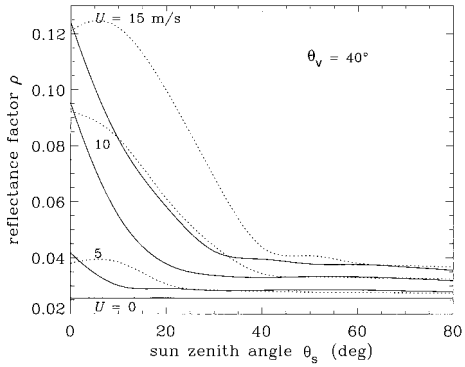

Fig. 9. Effect of wind speed and Sun zenith angle on ρ for a viewing direction of $\theta_v = 40$ deg and a clear-sky radiance distribution. The solid curves are for an azimuthal viewing direction of $\phi_v = 135$ deg and the dotted curves are for $\phi_v = 90$ deg.

used in Eq. (6). For $(\theta_v, \phi_v) = (40°, 135°)$ and clear skies, ρ is almost independent of wavelength because there is negligible Sun glint, and both the angular pattern of the sky radiance and the water index of refraction are nearly independent of wavelength. For $(\theta_v, \phi_v) = (30°, 90°)$, there is a factor of 2 wavelength dependence in ρ at $U = 10$ m s^{-1} because the white Sun glint has a different spectral dependence than the reflected blue sky radiance.

5. Dependence of ρ on Clouds

The simulations above were all for a clear sky as modeled by the Harrison and Coombes[11] formulas for a cloud parameter of $C = 0$ (C ranges from 0 for clear skies to 1 for heavy overcast). However, if clouds are present in the portion of the sky being reflected into the detector viewing the sea surface, then the value ρ will change because clouds are generally brighter than the background sky and thus give cloud glitter effects in analogy to Sun glitter.

To investigate the effects of clouds on ρ, I simulated idealized clouds in Hydrolight by simply increasing the Harrison and Coombes clear-sky radiance by a factor C_L for selected directions representing the locations of the clouds. Figure 10 shows the normalized clear-sky radiance distribution (contour lines) and the region of sky seen for a 10-m s^{-1} wind (points) as in Fig. 5. As in Figs. 2 and 5, the small rectangle shows the region of the sky that would be imaged for a level sea surface and that is used to measure L_s as in Fig. 1. The shaded areas of panels 1, 2, and 3 in Fig. 10 represent the locations of clouds in the Hydrolight quad partitioning of the sky. Cloud 1 represents a single cumulus cloud in an otherwise clear sky; cloud 2 represents a bank of clouds covering much of the horizon, and cloud 3 represents several cumulus clouds in the relevant part of the sky. Panel 4 shows the sky radiance for a uniformly overcast sky with $C = 0.5$ in the Harrison and Coombes formulas.

To obtain an idea of what values to use for C_L in the Hydrolight simulations, MODTRAN[14] Version 4.0 was used first to generate the clear-sky spectral radiance

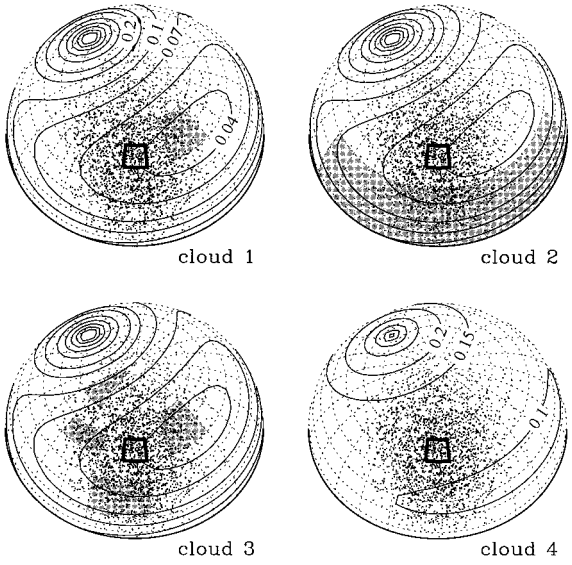

Fig. 10. Representations of clouds. The shaded areas in panels 1, 2, and 3 show the locations of clouds in an otherwise clear sky (sky radiance contours as in Fig. 5); panel 4 shows the sky radiance distribution for a cloud parameter value of $C = 0.5$ in the Harrison and Coombes[11] formulas. The Sun is at $\theta_s = 30$ deg and the viewing direction is $(\theta_v, \phi_v) = (40°, 135°)$. As in Figs. 2 and 5, the small rectangle shows the region of the sky that would be seen by a detector for zero wind speed, and the dots illustrate the region of the sky seen for a 10-m s^{-1} wind (2,000 points plotted).

at sea level corresponding to the viewing geometry seen in Fig. 10. Typical values were used for atmospheric parameters, e.g., 1976 U.S. Standard Atmosphere profiles with an open-ocean marine aerosol profile in the boundary layer, and azimuthally dependent multiple scattering was used in the radiance calculations. The computed clear-sky radiance L_s (at the centers of the small rectangles in Fig. 10) is shown in Fig. 11. The apparent radiance of a bright white cumulus cloud was then simulated as follows. The MODTRAN-computed spectral irradiance at 2-km altitude, E_c, was taken as being incident onto the vertical side of the cloud. The cloud was assumed to be a Lambertian reflector with an albedo of 80% so

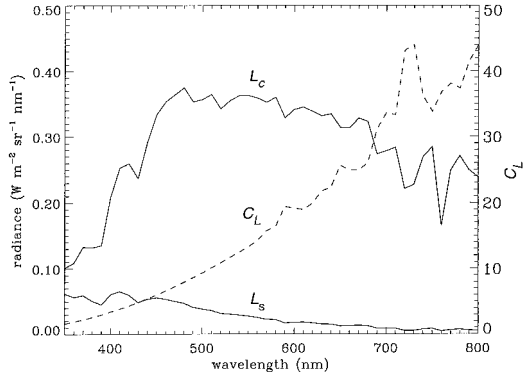

Fig. 11. MODTRAN-simulated blue-sky (L_s) and cumulus cloud (L_c) radiances for the viewing geometry of Fig. 10. The dashed curve shows the ratio $C_L = L_c/L_s$.

that the radiance leaving the cloud was $(0.8/\pi)E_c$. This radiance was then propagated to the sea surface by use of the MODTRAN-computed spectral transmittance along the slant path from the cloud to the sea surface. The resulting cloud radiance L_c is also shown in Fig. 11. The factor C_L is then just the ratio L_c/L_s. As can be seen in Fig. 11, C_L varies from less than 2 at 350 nm to more than 40 at 800 nm. This suggests that Hydrolight runs made with C_L values up to 50 would simulate the possible range of cloud radiances that might be encountered in nature. [The dashed curve of Fig. 11 is well described by a quadratic function of λ, except near 730 nm. Such a function was used for $C_L(\lambda)$ in the simulations for Fig. 14 below.]

Table 1 shows the values of C_L used for various simulations of clouds in an otherwise clear sky, along with the resulting ρ values. For this wind speed of 10 m s^{-1} and Sun and viewing geometry, the clear-sky ρ value is 0.0337. For the single cloud labeled cloud 1 in Fig. 10, ρ increases to 0.0361 for $C_L = 5$, i.e., for the cloud having five times the radiance of the clear sky in the same direction, as is typical at blue wavelengths. The value of ρ reaches 0.0635 for $C_L = 50$, which is possible at infrared wavelengths. Thus, depending on wavelength, the proper value to use for ρ varies by almost a factor of 2. The situation is even worse for cloud 2, which represents a cloud bank near the horizon: ρ now ranges from 0.0459 for $C_L = 5$ to 0.1835 for $C_L = 50$. This cloud has a greater effect on ρ both because it is larger and because its location near the horizon means that its radiance is reflected into the sensor more strongly because the Fresnel reflectances are larger for the wave facets that reflect near-horizon radiances into the sensor. The cumulus clouds arranged as in cloud 3 give ρ values that are similar to those of the cloud 1 case. A uniformly overcast sky, which is represented by the cloud 4 case, gives almost no change in ρ as the cloud cover increases (i.e., as the cloud parameter C of the Harrison and Coombes formulas increases). The minimum value of $\rho = 0.0248$ occurs when there is a heavy overcast: In this case the sky is fairly uniform and there is no Sun glint at all.

Additional and more realistic cloud simulations could be made. However, the results of a comprehensive study of randomly arranged clouds of various types likely would have to be presented in statistical form, which would still leave the user uncertain of what ρ value should be used for the clouds present during a particular observation. The simulations presented are sufficient to reach the conclusion that the ρ value to be used in correcting for surface-reflected sky radiance is strongly dependent on sky conditions, viewing geometry, sea state, and sometimes wavelength. Bear in mind that there are additional complications not modeled above, such as the effects of gravity waves or whitecaps, which will increase the uncertainty in ρ even more. Even though the uncertainty in ρ can be minimized by a judicious choice of viewing directions, it is still difficult for a researcher in the field to guess the correct value of ρ to use in Eq. (6), especially if clouds have introduced a wavelength dependence into ρ.

6. Effects of Errors in ρ on Estimated R_{rs}

Given that even an educated guess for ρ may be in error by a factor of 2 or more when Eq. (6) is used, it is necessary to investigate the consequence of such errors in ρ on the estimation of R_{rs}. As is clear from Eq. (6), if L_t is dominated by L_w, then imprecise correction for sky radiance may be of little importance. On the other hand, if the reflected sky radiance is much greater than the water-leaving radiance, then any error in removing the sky radiance may be significant. The relative contributions of L_w and L_r to L_t depend on the water absorption and scattering properties, and thus on wavelength, as well as on viewing geometry.

Table 1. Simulations of Cloud Effects on ρ[a]

Cloud Case	C_L	C	ρ	Comment
No clouds	1.0	0.0	0.0337	Clear sky
Cloud 1	5.0	0.0	0.0361	Single cumulus cloud; 400 nm
	10.0	0.0	0.0392	Single cumulus cloud; 500 nm
	20.0	0.0	0.0452	Single cumulus cloud; 600 nm
	50.0	0.0	0.0635	Single cumulus cloud; 700–800 nm
Cloud 2	5.0	0.0	0.0459	Cloud bank on horizon; 400 nm
	10.0	0.0	0.0612	Cloud bank on horizon; 500 nm
	20.0	0.0	0.0918	Cloud bank on horizon; 600 nm
	50.0	0.0	0.1835	Cloud bank on horizon; 700–800 nm
Cloud 3	5.0	0.0	0.0363	Scattered cumulus clouds; 400 nm
	10.0	0.0	0.0396	Scattered cumulus clouds; 500 nm
	20.0	0.0	0.0462	Scattered cumulus clouds; 600 nm
	50.0	0.0	0.0659	Scattered cumulus clouds; 700–800 nm
Cloud 4	—	0.25	0.0286	Thin uniform overcast
	—	0.50	0.0264	Increasing overcast
	—	0.75	0.0254	Increasing overcast
	—	1.0	0.0248	Thick overcast, no Sun visible

[a]The wind speed was 10 m s^{-1}. The locations of the clouds are shown in Fig. 10. Cloud parameters C_L and C are described in the text.

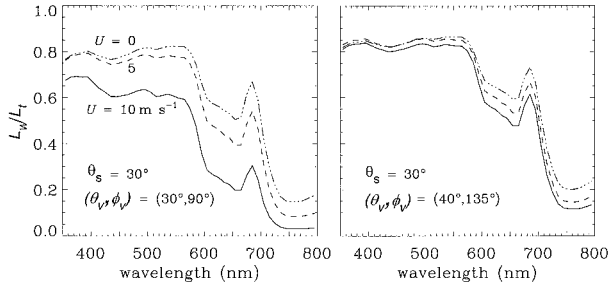

Fig. 12. Relative contribution of the water-leaving radiance L_w to the total upward radiance L_t as a function of wind speed U and wavelength for a case 1 water body with 2 mg m^{-3} of chlorophyll and for $\theta_s = 30$ deg in a clear sky. The left panel is for a viewing direction of $(\theta_v, \phi_v) = (30°, 90°)$ and the right panel is for $(\theta_v, \phi_v) = (40°, 135°)$.

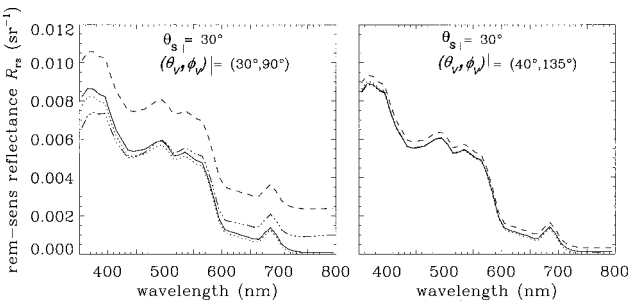

Fig. 13. Exact and estimated R_{rs} for a wind speed of $U = 10$ m s^{-1} and for $\theta_s = 30$ deg in a clear sky. The left panel is for a viewing direction of $(\theta_v, \phi_v) = (30°, 90°)$ and the right panel is for $(\theta_v, \phi_v) = (40°, 135°)$. The water body is the same as for Fig. 12. The curve patterns denote the exact R_{rs} (solid curves); R_{rs} is estimated by use of $\rho = 0.0222$ (dashed curves), $\rho = 0.06$ in Eq. (6) (left panel, dash–dot curve), or $\rho = 0.034$ in Eq. (6) (right panel, dash–dot curve); and the SeaWiFS estimate is based on Eq. (7) (dotted curves).

To illustrate this dependence, a homogeneous water body with a chlorophyll concentration of 2 mg m^{-3} was simulated by use of bio-optical models for the absorption[15] and scattering[16] coefficients of case 1 waters, as built into Hydrolight. Hydrolight computes the reflected-sky and water-leaving radiances separately, which makes it an ideal tool for evaluating Eqs. (1) and (6) because there is no uncertainty in how the computed L_t is partitioned into L_w and L_s. The left panel of Fig. 12 shows the ratio of the Hydrolight-generated clear-sky water-leaving radiance to total radiance L_w/L_t as a function of wind speed and wavelength for $\theta_s = 30$ deg and for the traditional viewing direction of $(\theta_v, \phi_v) = (30°, 90°)$. We can see that the contribution of L_w to the measurable radiance can range from over 80% at low wind speeds and blue to green wavelengths to less than 20% at red wavelengths at high wind speeds. The relative contribution of L_w to the total decreases as the wind speed increases because wave facets reflect more of the brighter, near-Sun sky into the detector. All Hydrolight simulations included Raman scatter by the water and chlorophyll and chromophoric dissolved organic matter fluorescence, which for these water conditions noticeably affect only the chlorophyll fluorescence band near 685 nm. The right panel of Fig. 12 shows L_w/L_t for the same simulation, but for a viewing direction of $(\theta_v, \phi_v) = (40°, 135°)$ as recommended above in the discussion of ρ. The ratio of L_w to L_t is now somewhat higher at all wavelengths, and the ratio is less dependent on wind speed because there is less Sun glitter for the (40°, 135°) viewing direction. Note that even though this is a simulation of case 1 water, the water-leaving radiance is not zero at 750 nm and can be as much as 20% of the total upwelling radiance above the surface at 750 nm for the water conditions of this simulation. This is consistent with observations.[17]

Figure 13 shows the exact and estimated R_{rs} for the same simulation as used in Fig. 12 for the 10-m s^{-1} wind. Here exact refers to the value of L_w/E_d computed with the Hydrolight-generated values of L_w and E_d, and estimated refers to R_{rs} as obtained from Eq. (6), again with Hydrolight-generated radiances. The left panel shows estimates of R_{rs} based on the traditional viewing geometry of $(\theta_v, \phi_v) = (30°, 90°)$. The solid curve shows the exact R_{rs} computed from L_w/E_d. The dashed curve is the estimate of R_{rs} obtained by use of $\rho = 0.0222$ (the Fresnel reflectance for $\theta_v = 30°$) in Eq. (6), as recommended by the SeaWiFS protocol.[4] The estimated R_{rs} is greater than the true R_{rs} because, as can be seen in Figs. 6 or 8, the correct ρ value for this geometry is approximately 0.06; use of a value of 0.0222 therefore removes too little of the reflected sky radiance, making the numerator of Eq. (6) too large. The dotted curve is the SeaWiFS estimate obtained from our subtracting the value at 750 nm from the dashed curve. This gives the final estimate of R_{rs} by Eq. (7), which is seen to be quite close to the exact R_{rs}. The dash–dot curve in the left panel is the estimate of R_{rs} obtained by use of $\rho = 0.06$, in Eq. (6), as estimated from Fig. 8. Use of this better guess for ρ improves the estimate when Eq. (6) is used, although the agreement is not as good as that of Eq. (7). The exact values of ρ that should be used in Eq. (6) varied from 0.0425 at 350 nm to 0.0850 at 800 nm. This wavelength dependence of the clear-sky ρ results from the different wavelength dependencies of the white Sun glitter and the blue-sky radiance, just as discussed above for clouds. Use of $\rho = 0.06$ thus removes too much reflected radiance at blue wavelengths and too little at red wavelengths, as can be seen in Fig. 13.

These simulations are consistent with the conclusions of Toole *et al.*,[18] who did a detailed comparison of R_{rs} spectra determined from empirical data by several methodologies based on Eqs. (6), (7), and (10). They used the traditional viewing direction of $\phi_v = 90$ deg in the application of Eq. (6). They concluded that "It seems likely that the reflected sky radiance is severely underestimated following these protocols." That is to say, use of a value of $\rho \approx 0.02$ or 0.03 in Eq. (6) is incorrect at higher wind speeds.

The right panel of Fig. 13 shows the exact and estimated R_{rs} for the recommended viewing geometry

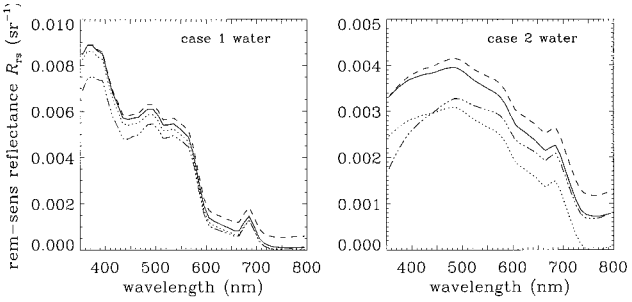

Fig. 14. Exact and estimated R_{rs} for a wind speed of $U = 10$ m s^{-1} and for $\theta_s = 30$ deg in a sky with clouds arranged as in the cloud 3 case of Fig. 10. Both panels have $(\theta_v, \phi_v) = (40°, 135°)$. The left panel is for case 1 water and the right panel is for case 2 water, as described in the text. In both panels the curves denote the exact R_{rs} (solid curves), estimates made with $\rho = 0.0332$ (dashed curves and $\rho = 0.0595$ (dash–dot curves) and the SeaWiFS estimate (dotted curves).

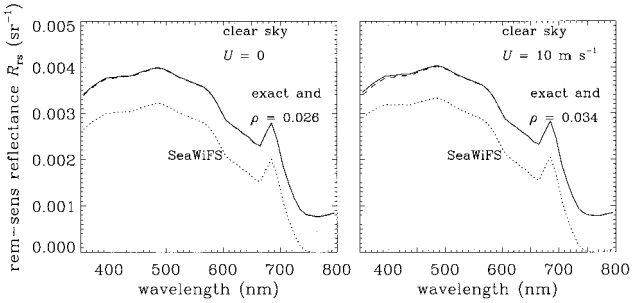

Fig. 15. Exact and estimated R_{rs} for a wind speeds of $U = 0$ and 10 m s^{-1} for $\theta_s = 30$ deg in a clear sky. The water body is the case 2 water described in the text. The curve patterns denote the exact R_{rs} (solid curves) the estimate made with Eq. (6) and the appropriate ρ value from Fig. 9 (dashed curves) and the SeaWiFS estimate (dotted curves). The bars at the bottom of the left panel show the nominal SeaWiFS bands.

of $(\theta_v, \phi_v) = (40°, 135°)$. The dashed curve shows the estimate obtained from Eq. (6) by use of the Fresnel reflectance of 0.0253 (the value for $\theta_v = 40°$) for ρ; this value is quite close to the exact value. Use of a value of $\rho = 0.034$, as obtained from Fig. 9 for this wind speed and solar angle, yields an estimate of R_{rs} that is almost indistinguishable from the exact value. (This value of ρ varies by less than 4% over the 350–800-nm range because there is negligible Sun glint for this viewing geometry.) Likewise, the final SeaWiFS estimate is excellent. For wind speeds of 5 m s^{-1} or less (figures not shown), the agreement between the exact and estimated (by use of $\rho = 0.0253$) R_{rs} is even better, because $\rho = 0.0253$ is close to the correct value for both viewing geometries.

Figure 14 shows two simulations for a 10-m s^{-1} wind and cloud case 3 as shown in Fig. 10. The viewing direction is $(\theta_v, \phi_v) = (40°, 135°)$ in both panels. The left panel is the same case 1 water as was used in Fig. 13; only the sky conditions have been changed to include clouds. The right panel also is for the cloud 3 sky conditions, but for a simulation of turbid case 2 water. This water body had a chlorophyll concentration of 5 mg m^{-3}, a chromophoric dissolved organic matter concentration that gave absorption at 440 nm that was comparable to absorption by chlorophyll [namely, $a_{CDOM}(440\text{ nm}) = 0.25$ m^{-1}], and mineral particles consistent with a concentration of 10 g m^{-3} of clay particles[19,20] [namely, $a_{min}(440\text{ nm}) = 1.0$ m^{-1} and $b_{min}(440\text{ nm}) = 5.0$ m^{-1}]. The mineral particles were modeled with a wavelength-independent absorption coefficient and a scattering coefficient that varied as $1/\lambda$. The high concentrations of biological and mineral particles in this simulation made the water-leaving radiance at 750 nm comparable with that of the surface-reflected sky radiance.

As before, the solid line shows the exact R_{rs}. Because of the clouds, the value of ρ varies from 0.0332 at 350 nm to 0.0595 at 800 nm. The dashed curves show the estimates of R_{rs} by use of $\rho = 0.0332$ in Eq. (6), and the dash–dot curves show the estimates using $\rho = 0.0595$. These two curves highlight the effect of the cloud-induced spectral dependence of ρ, which is especially noticeable for the case 2 water. The dotted curves show the SeaWiFS estimate based on Eq. (7) and a ρ value of 0.0253. The SeaWiFS estimate is quite good for the case 1 water, but is much too low for the case 2 water because the assumption of zero water-leaving radiance at 750 nm is not satisfied. Figure 9 gives a ρ value of approximately 0.034, which generates an estimate that is indistinguishable from the dashed curves in Fig. 14. Thus, for this particular case 2 water body, an estimate based on Eq. (6) is much better than the corrected estimate based on Eq. (7).

The result just discussed, namely, that Eq. (6) can give better estimates than Eq. (7) for case 2 water, holds for other sky conditions and wind speeds. Figure 15 shows simulations for the same case 2 water body, but for clear skies with wind speeds of $U = 0$ and 10 m s^{-1}. Figure 9 gives $\rho = 0.026$ for $U = 0$ and 0.034 for $U = 10$ m s^{-1}. Use of these clear-sky values in Eq. (6) yields R_{rs} estimates that are almost indistinguishable from the exact values, whereas Eq. (7) always yields a less accurate estimate because the water-leaving radiance is not zero at 750 nm.

Even in the worst cases of Figs. 14 and 15, the spectral shape of R_{rs} is fairly well preserved; only the magnitude is in error. This situation may be acceptable for some applications. However, significant errors can arise when taking the ratio of R_{rs} at two different wavelengths, especially if ratioing blue-green to orange-red wavelengths. For example, although the ratio $R_{rs}(445)/R_{rs}(555)$ is in error by less than 1% for the SeaWiFS curves of Fig. 15, $R_{rs}(555)/R_{rs}(670)$ is off by 25%.

Although it is difficult to generalize from the limited simulations made here, Figs. 12–15 do suggest the following: (1) a viewing direction of $(\theta_v, \phi_v) = (40°, 135°)$ yields less Sun glint and thus less noise in estimates of R_{rs} than does the traditional direction of

$(\theta_v, \phi_v) = (30°, 90°)$ (Figs. 12 and 13); (2) although the SeaWiFS protocol of Eq. (7) can give satisfactory results in case 1 waters, it can give biased results in waters where the water-leaving radiance at 750 nm is not close to zero (Figs. 14 and 15); and (3) an R_{rs} estimate based on Eq. (6) and the ρ values of Fig. 9 can give less biased estimates than Eq. (7) in waters where the water-leaving radiance at 750 nm is not zero (Figs. 14 and 15).

7. Recommendations for Estimating R_{rs}

The simulations presented above show that it is difficult to determine the correct value of the reflectance $\rho(\lambda)$ that should be used to remove the surface-reflected skylight from a measured total radiance. Nevertheless, both the simulations of Section 6 and the established success of use of Eqs. (6) and (7) with $\rho \approx 0.028$ indicate that the errors induced in the estimated R_{rs} by use of incorrect ρ values are often, but not always (e.g., Figs. 14 and 15), small. There is certainly room for improvement over this method of estimating the remote-sensing reflectance.

Lee *et al.*[21] recently proposed a new protocol for the estimation of R_{rs}. Their method partitions the skylight into Rayleigh and aerosol components. The radiance distribution arising from Rayleigh scattering is assumed to be uniform, so that its contribution to L_t can be removed by use of a ρ value, ρ_{ray}, corresponding to a completely uniform sky, i.e., a sky without any Sun present. The contributions of aerosol scattering, which make the sky bright in the vicinity of the Sun, and of glitter by the Sun's direct beam are then removed from L_t by a sophisticated optimization procedure that makes use of data over the broad spectral range from 400 to 830 nm. Lee *et al.* suggest using a value of $\rho_{ray} \approx 0.021$ for the removal of the Rayleigh component of the reflected skylight when the viewing angle is $\theta_v = 30°$. Hydrolight-generated ρ values for a completely uniform sky (not shown here; see Mobley and Stramski[22]) show that in this case the wind speed has little effect on ρ and that use of a value of 0.021 or 0.022 for ρ_{ray} is justified. The optimization method of Lee *et al.* (or some similar algorithm) may prove to be a significant improvement over the traditional ways of estimating R_{rs}. Likewise, the advantages of using polarizers to reduce reflected skylight are becoming established.[13,17,23]

However, until an improved method of estimating R_{rs} becomes available and accepted, the following suggestions can be made for using the traditional method based on Eq. (6).

A viewing direction of $\theta_v \approx 40°$ from the nadir and $\phi_v \approx 135°$ from the Sun will minimize the effects of Sun glint and nonuniform sky radiance while also avoiding instrument shading problems. For this viewing direction, a value of $\rho \approx 0.028$ is acceptable for wind speeds less than 5 m s^{-1}. At higher wind speeds, the clear-sky ρ value should be increased in accordance with Fig. 9. If the sky is heavily overcast, use a value of $\rho \approx 0.028$ at all wind speeds. There is little justification for attempting to be more precise than this in practice, especially if clouds are present. Although residual Sun glint effects can be further corrected in some cases by subtracting the value of $R_{rs}(750\ nm)$ as suggested in the SeaWiFS protocol, this procedure will yield less accurate estimates in highly scattering waters than those based solely on Eq. (6) and the ρ values of Fig. 9.

This research was supported by the Environmental Optics Program of the U.S. Office of Naval Research and by the Remote Sensing Division of the Naval Research Laboratory. Dave Siegel and Tonya Clayton made helpful suggestions on an early version of the manuscript.

References

1. C. D. Mobley, *Light and Water: Radiative Transfer in Natural Waters* (Academic, San Diego, Calif., 1994).
2. C. D. Mobley, B. Gentili, H. R. Gordon, Z. Jin, G. W. Kattawar, A. Morel, P. Reinersman, K. Stamnes, and R. H. Stavn, "Comparison of numerical models for computing underwater light fields," Appl. Opt. **32,** 7484–7504 (1993).
3. C. D. Mobley, *Hydrolight 4.0 Users' Guide*, Second Printing (Sequoia Scientific, Inc., Redmond, Wash., 1998).
4. J. L. Mueller and R. W. Austin, "Ocean optics protocols for SeaWiFS validation, revision 1," SeaWiFS Technical Report Series, Vol. 25, NASA Tech. Memo. 104566, S. B. Hooker, E. R. Firestone, and J. G. Acker, eds. (National Technical Information Service, Springfield, Va., 1995).
5. K. L. Carder and R. G. Steward, "A remote-sensing reflectance model of a red-tide dinoflagellate off west Florida," Limnol. Oceanogr. **30**(2), 286–298 (1985).
6. J. R. V. Zaneveld, "An asymptotic closure theory of irradiance in the sea and its inversion to obtain the inherent optical properties," Limnol. Oceanogr. **34,** 1442–1452 (1989).
7. R. W. Preisendorfer and C. D. Mobley, "Albedos and glitter patterns of a wind-roughened sea surface," J. Phys. Oceanogr. **16,** 1293–1316 (1986).
8. H. R. Gordon, O. B. Brown, R. H. Evans, J. W. Brown, R. C. Smith, K. S. Baker, and D. C. Clark, "A semianalytic radiance model of ocean color," J. Geophys. Res. **93**(D9), 10,909–10,924 (1988).
9. A. Morel and B. Gentili, "Diffuse reflectance of oceanic waters. II. Bidirectional aspects," Appl. Opt. **32,** 6864–6879 (1993).
10. A. Morel, K. J. Voss, and B. Gentili, "Bidirectional reflectance of oceanic waters: a comparison of modeled and measured upward radiance fields," J. Geophys. Res. **100**(C7), 13,143–13,150 (1995).
11. A. W. Harrison and C. A. Coombes, "An opaque cloud cover model of sky short wavelength radiance," Sol. Energy **41**(4), 387–392 (1988).
12. R. W. Austin, "Inherent spectral radiance signatures of the ocean surface," in S. Q. Duntley, R. W. Austin, W. H. Wilson, C. F. Edgerton, and S. E. Moran, "Ocean color analysis," SIO Ref. 74-10 (Scripps Institution of Oceanography, La Jolla, Calif., 1974).
13. B. Fougnie, R. Frouin, P. Lecomte, and P.-Y. Deschamps, "Reduction of skylight reflection effects in the above-water measurement of diffuse marine reflectance," Appl. Opt. **38,** 3844–3856 (1999).
14. P. K. Acharya, A. Berk, L. S. Bernstein, M. W. Matthew, S. M. Adler-Golden, D. C. Robertson, G. P. Anderson, J. H. Chetwynd, F. X. Kneizys, E. P. Shettle, L. W. Abreu, W. O. Gallery, J. E. A. Selby, and S. A. Clough, "MODTRAN user's manual versions 3.7 and 4.0" (Air Force Research Laboratory, Space Vehicles Directorate, Hanscom Air Force Base, Mass., 1998).
15. A. Morel, "Light and marine photosynthesis: a spectral

model with geochemical and climatological implications," Prog. Oceanogr. **26,** 263–306 (1991).
16. H. R. Gordon and A. Morel, "Remote assessment of ocean color for interpretation of satellite visible imagery, a review," in *Lecture Notes on Coastal and Estuarine Studies* (Springer Verlag, New York, 1983), Vol. 4.
17. M. Sydor, R. A. Arnone, R. W. Gould, Jr., G. E. Terrie, S. D. Ladner, and C. G. Wood, "Remote-sensing technique for determination of the volume absorption coefficient of turbid water," Appl. Opt. **37,** 4944–4950 (1998).
18. D. A. Toole, D. A. Siegel, D. W. Menzies, J. J. Neumann, and R. C. Smith, "Remote sensing reflectance determinations in coastal environments—impacts of instrumental characteristics and environmental variability," Appl. Opt. (to be published).
19. C. H. Whitlock, L. R. Poole, J. W. Usry, W. M. Houghton, W. G. Witte, W. D. Morris, and E. A. Gurganus, "Comparison of reflectance with backscatter and absorption parameters for turbid waters," Appl. Opt. **20,** 517–522 (1981).
20. R. P. Bukata, J. H. Jerome, K. Ya. Kondratyev, and D. V. Pozdnyakov, *Optical Properties and Remote Sensing of Inland and Coastal Waters* (CRC Press, New York, 1995).
21. Z. P. Lee, K. L. Carder, R. G. Steward, T. G. Peacock, C. O. Davis, and J. L. Mueller, "Remote-sensing reflectance and inherent optical properties of oceanic waters derived from above-water measurements," in *Ocean Optics XIII*, S. G. Ackleson and R. Frouin, ed., Proc. SPIE **2963,** 160–166 (1997).
22. C. D. Mobley and D. Stramski, "Origins of variability in remote-sensing reflectances," Final Report (Sequoia Scientific, Inc., Redmond, Wash., 1997).
23. M. Sydor and R. A. Arnone, "Effect of suspended particulate and dissolved organic matter on remote sensing of coastal and riverine waters," Appl. Opt. **36,** 6905–6912 (1997).